Control of Net Radiative Heat Transfer With a Variable-Emissivity Accordion Tessellation

Rydge B. Mulford
Department of Mechanical Engineering,
Brigham Young University,
Provo, UT 84602

Vivek H. Dwivedi
NASA Goddard Space Flight Center,
Greenbelt, MD 20771

Matthew R. Jones
Department of Mechanical Engineering,
Brigham Young University,
Provo, UT 84602

Brian D. Iverson[1]
Department of Mechanical Engineering,
Brigham Young University,
Provo, UT 84602
e-mail: bdiverson@byu.edu

Origami tessellations have been proposed as a mechanism for control of radiative heat transfer through the use of the cavity effect. This work explores the impact of a changing projected surface area and varying apparent radiative properties on the net radiative heat transfer of an accordion fold comprised of V-grooves. The net radiative heat transfer of an accordion tessellation is obtained by a thermal energy balance at the cavity openings with radiative properties of the cavities given as a function of various cavity parameters. Results of the analytical model are experimentally confirmed. An accordion tessellation, constructed of stainless-steel shim stock, is positioned to achieve a specified fold angle and placed in a vacuum environment while heated by Joule heating. A thermal camera records the apparent temperature of the cavity openings for various fold angles. Results are compared to apparent temperatures predicted with the analytical model. Analytically and experimentally obtained temperatures agree within 5% and all measurements fall within experimental uncertainty. For diffusely irradiated surfaces, the decrease in projected surface area dominates, causing a continuous decrease in net radiative heat transfer for a collapsing accordion fold. Highly reflective specular surfaces exposed to diffuse irradiation experience large turn-down ratios (7.5× reduction in heat transfer) in the small angle ranges. Specular surfaces exposed to collimated irradiation achieve a turn down ratio of 3.35 between V-groove angles of 120 deg and 150 deg. The approach outlined here may be extended to modeling the net radiative heat transfer for other origami tessellations. [DOI: 10.1115/1.4042442]

Keywords: origami, variable emissivity, net surface heat transfer, accordion, V-groove

Introduction

The static behavior of radiative surface properties can prevent optimal operation of thermal management systems that are dominated by radiative heat transfer. As an example, consider a spacecraft in low earth orbit [1]. Variations in spacecraft power dissipation and large external heating variations can result in significant fluctuations in heat loss. However, because the spacecraft radiator's surface properties and emitting area are inherently static, radiators are designed to reject the maximum heat load experienced by the spacecraft. Power consuming heaters are commonly utilized to maintain desired operating temperatures [1,2], increasing the size, weight, and power of the spacecraft equipment. An alternative solution is to provide a radiator with dynamically variable radiative surface properties, giving the radiator the ability to adjust radiative heat loss in response to a change in operating conditions. Such a radiator would be possible with variable emissivity devices.

Several experimental variable emissivity devices exist [3,4], including electrochromic [5–11] and thermochromic [12–14] coatings. Utilizing changes to internal chemistry through applied voltages or temperature changes, these devices exhibit a change in emissivity as large as one order of magnitude [14]. However, these surfaces have not yet shown satisfactory performance in a vacuum setting [2,4,15]. As such, another approach to variable emissivity has been proposed [16–18], utilizing origami tessellations and the cavity effect.

The cavity effect describes the increased absorbing and emitting capabilities of cavities as compared to flat surfaces. Radiation entering a cavity of any given geometry may be reflected multiple times before potentially exiting the cavity. These inter-reflections result in a greater fraction of absorbed irradiation as compared to a flat surface with an equivalent size as the cavity opening and an absorptivity are equal to that of the cavity material. Likewise, the emissivity of the cavity opening is greater than the intrinsic emissivity of the cavity material. The extent of the cavity effect is quantified with apparent absorptivity and apparent emissivity [19]. Apparent emissivity for an isothermal cavity is defined as the ratio of the emitted heat rate from a real cavity opening as compared to the emitted heat rate from a similar cavity (same temperature and geometry) but with surfaces that have an intrinsic emissivity of unity. Apparent absorptivity is defined as the ratio of irradiation absorbed by the cavity compared to the total irradiation incident on the cavity opening [20].

Apparent radiative properties for a given cavity are a function of several parameters including cavity geometry, intrinsic radiative surface properties, reflection type (specular/diffuse), irradiation type, and boundary conditions [21,22]. As such, the apparent radiative surface properties of a cavity may be controlled by changing one or more of these parameters. Physical actuation of origami tessellations may be used to achieve variation in apparent radiative properties through a changing cavity geometry [16–18,23,24]. For example, as an accordion tessellation (Fig. 1) is collapsed, the aspect ratio of the V-groove cavities increases, causing the apparent emissivity and apparent absorptivity of the

[1]Corresponding author.

Contributed by the Heat Transfer Division of ASME for publication in the Journal of Heat Transfer. Manuscript received August 8, 2018; final manuscript received December 17, 2018; published online January 30, 2019. Assoc. Editor: Thomas Beechem.

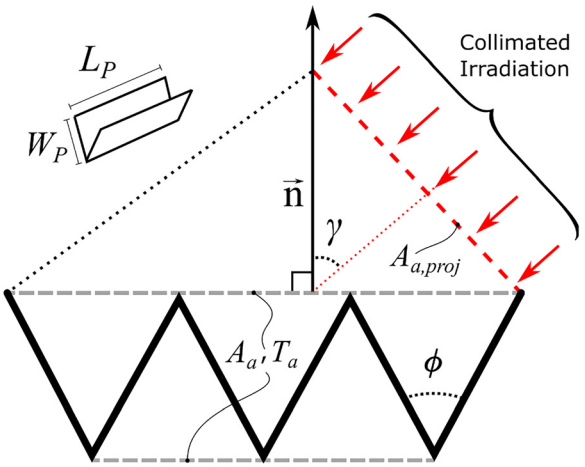

Fig. 1 Geometric features of the accordion tessellation, including the cavity angle ϕ, tessellation length L_P, tessellation width W_P, projected area of the cavity openings normal to collimated irradiation $A_{a,proj}$, apparent surface area of the tessellation A_a, apparent temperature T_a, and the collimated irradiation angle of incidence γ

cavities to increase. Any origami tessellation with variable cavity geometries, such as the Miura-Ori or Barreto's Mars tessellations [18,25], is capable of variable emissivity through this same mechanism.

However, the apparent radiative properties of a tessellation are not the only changing variables affecting the net heat transfer rate. As a tessellation is actuated to modify the apparent radiative properties, the apparent emitting area of the cavity openings likewise changes. For most tessellations, the apparent surface area decreases toward zero as apparent radiative properties increase, with some exceptions such as Barreto's Mars tessellation [25]. Published works that explore origami tessellations and the cavity effect have only considered the effect of a tessellation change on apparent radiative properties and have not addressed the effect of a changing apparent surface area on net radiative heat transfer [17,23,24].

The purpose of this work is to quantify the net radiative heat exchange of an accordion origami tessellation as a function of actuation position. The accordion tessellation was selected to utilize the existing models that describe apparent emissivity and apparent absorptivity for an infinite V-groove [20,23,24,26]. However, the analytical approach has been generalized to allow for application to any origami tessellation if a model of the apparent radiative properties can be obtained or developed. This work will consider specularly or diffusely reflecting surfaces as well as collimated or diffuse irradiation from the surroundings; such conditions are representative of the thermal environment encountered in space applications.

A general energy balance is developed to predict the net radiative heat transfer for any origami tessellations. This energy balance is then applied to the accordion tessellation. Next, an experimental method used to verify the results from the analytical model is described, and this is followed by a discussion of the uncertainties for both the analytical and experimental approaches. Results from the analytical model are presented for diffuse or collimated irradiation and for a diffuse or specular reflector, illustrating the net radiative heat transfer behavior of an accordion tessellation as a function of geometry. The analytical results are compared to the experimental results for validation in predicting net radiative heat exchange of the accordion tessellation. Finally, implications of the results for net radiative heat exchange with regard to use of the accordion tessellation as a dynamic radiator are discussed.

Analytical Methods

General Energy Balance. Consider an isothermal origami tessellation, consisting of an array of cavities, suspended in space that is in radiative equilibrium with the surroundings. Emission from the origami tessellation is assumed to be diffuse but the tessellation surfaces may reflect either specularly or diffusely. The tessellation may receive irradiation from diffusely emitting surroundings and/or from collimated irradiation of a known heat flux (G) at some angle of incidence (γ) with respect to the apparent surface normal (Fig. 1). Net radiative heat exchange (q_{rad}) between the tessellation and the surroundings is a balance of emitted (q_e) and absorbed (q_{abs}) heat transfer rates, as given in the following equation:

$$q_{\text{rad}} = q_e - q_{\text{abs}} = \varepsilon_a A_a \sigma T_a^4 - [\alpha_a A_a \sigma T_{\text{surr}}^4 + \alpha_a A_{a,\text{proj}} G_{\text{collimated}}] \tag{1}$$

The apparent absorptivity (α_a) in Eq. (1) accounts for the reflections and rereflections of radiative power streaming into the cavity. Likewise, emission from the opening is modeled by assigning an apparent temperature to the cavity opening with a given apparent emissivity (ε_a) to account for the reflections and reabsorptions of emitted energy. The apparent area A_a is the planar surface area of all tessellation cavity openings and applies to diffuse emission and diffuse irradiation, whereas $A_{a,\text{proj}}$ is the apparent projected area of the array normal to the collimated irradiation (Fig. 1). These apparent properties and the apparent area are functions of tessellation geometry.

Accordion Tessellation. The net heat rate for an accordion tessellation using Eq. (1) may be obtained by defining the opening area of a single V-groove as a function of ϕ and multiplying by the number of cavity openings on the top and bottom of the surface, giving the apparent area in Eq. (2) as pictured in Fig. 1. For the apparent projected area, the apparent area of only the top surface is multiplied by the cosine of the collimation angle of incidence, resulting in Eq. (3). In Eqs. (2)–(3), W_P is the width of one panel and the panels are assumed to be of sufficient length (L_P) that end effects are neglected (e.g., $L_P/W_P \gg 1$). Emission from the bottom side of the panels furthest to the left and right is neglected in this analysis

$$A_a = 2(N_{\text{panels}} - 1) W_P L_P \sin\left(\frac{\phi}{2}\right) \tag{2}$$

$$A_{a,\text{proj}} = N_{\text{panels}} W_P L_P \sin\left(\frac{\phi}{2}\right)\cos(\gamma) \tag{3}$$

These area terms are then substituted into Eq. (1). After simplification, the net radiative heat exchange for an accordion tessellation experiencing irradiation from a diffuse source and/or collimated irradiation may be described with the following equation:

$$q_{\text{rad}} = 2W_P L_P \sin\left(\frac{\phi}{2}\right)\left[(N_{\text{panels}} - 1)\sigma\left(\varepsilon_a T_a^4 - \alpha_a T_{\text{surr}}^4\right) - \alpha_a G\left(\frac{N_{\text{panels}}}{2}\right)\cos(\gamma)\right] \tag{4}$$

Apparent Radiative Properties. Results for Eq. (4) require the apparent radiative properties (ε_a and α_a) as a function of intrinsic emissivity (ε), V-groove angle (ϕ), and irradiation incidence angle (γ), where applicable. Recalling that apparent absorptivity is dependent on the type of irradiation (diffuse irradiation versus collimated irradiation) and reflection (specular versus diffuse), four separate models for apparent absorptivity are necessary. Apparent emissivity is independent of the behavior of irradiation entering the cavity, and therefore, only two apparent emissivity models are required, one each for specular and diffuse reflection. Ohwada [27] has shown that the apparent emissivity of an

Table 1 Apparent emissivity and apparent absorptivity models for *specularly reflecting V-groove surfaces*

Property	Conditions	Reference	Specular reflection model
ε_a	Diffuse emission for an isothermal gray surface with *specular* reflection	[24,28]	$\varepsilon_a = \dfrac{\varepsilon}{\sin\left(\frac{\phi}{2}\right)}\left[1-\varepsilon\sum_{k=1}^{n}\rho^{k-1}\left(1-\sin\left(k\frac{\phi}{2}\right)\right)\right]$ $n=\dfrac{\phi}{2}$ where n is the integer portion of ϕ/π[a]
α_a	Diffuse irradiation on a gray surface with specular reflection	[27,28]	Same as above
α_a	Collimated irradiation with full-illumination ($\phi/2 \geq \gamma$) on a gray surface with specular reflection	[20,24]	$\alpha_a = \dfrac{\left[1-(1-\alpha X')(1-\alpha)^{n-1}\right]\sin\left(\frac{\phi}{2}+\gamma\right)+\left[1-(1-\alpha Y')(1-\alpha)^{m-1}\right]\sin\left(\frac{\phi}{2}-\gamma\right)}{2\cos(\gamma)\sin(\phi/2)}$ $n=\dfrac{(\pi-\gamma)}{\phi}+\dfrac{1}{2}\quad m=\dfrac{(\pi+\gamma)}{\phi}+\dfrac{1}{2}$ where n and m are rounded down[a] $X'=\dfrac{\sin[(n-1/2)\phi+\gamma]}{\sin(\phi/2+\gamma)}\quad Y'=\dfrac{\sin[(m-1/2)\phi-\gamma]}{\sin(\phi/2-\gamma)}$
α_a	Collimated irradiation with partial-illumination ($\phi/2 < \gamma$) on a gray surface with specular reflection	[24]	$\alpha_a = 1-(1-\alpha X')(1-\alpha)^{n-1}$ $n < \dfrac{\pi-2\gamma}{\phi}+1$ where n is rounded down[a] $X' = \dfrac{\sin[(n-1/2)\phi+\gamma]}{\sin(\phi/2+\gamma)}\quad X'' = \dfrac{\sin(\gamma-\phi/2)}{\sin(\pi-\phi/2-\gamma)}$ If $X' < X''$, then: $X' = 0$; If $X' > X''$, then: $X' = \dfrac{X'-X''}{1-X'}$

[a]The number of reflections (n and/or m) must be rounded down to the nearest whole number; if the calculation of n and/or m yields a whole number, that value should be deprecated by unity [24].

isothermal, diffusely emitting cavity is equivalent to the apparent absorptivity of a diffusely irradiated cavity regardless of the reflection type. As such, the apparent absorptivity models for diffuse irradiation likewise describe the apparent emissivity behavior for both specular and diffuse reflection.

Recent works [23,24] have built upon early models by Sparrow and Lin [20] and Modest [28] to obtain closed form models of apparent absorptivity and apparent emissivity of V-grooves for all possible combinations of surface conditions and irradiation types. A summary of these models is given in Tables 1 and 2. These models assume infinite V-grooves with isothermal cavities in order for the apparent absorptivity and apparent emissivity to be equated through Ohwada's proof [27]. Although real tessellations cannot extend indefinitely, V-grooves with panel length to width ratios of ten or greater ($L_P/W_P > 10$) exhibit apparent radiative properties to within ~5% of infinite V-groove values [18].

With the appropriate areas defined, the net radiative heat transfer for an accordion fold can be obtained with Eq. (4) using models for the apparent radiative properties from Tables 1 and 2. These properties may be dynamically altered through actuation to

Table 2 Apparent emissivity and apparent absorptivity models for *diffusely reflecting V-groove surfaces*. Infinite summations should be carried out to at least twenty terms for accuracy [23].

Property	Conditions	Reference	Diffuse reflection model
ε_a	Diffuse emission for an isothermal gray surface with *diffuse* reflection	[23]	$\varepsilon_a = \varepsilon\Lambda_1(\varepsilon,\phi)\sum_{n=0}^{\infty}(1-\varepsilon)^n\left[1-\sin\left(\frac{\phi}{2}\right)\right]^n$ Approximate with > 20 terms $\Lambda_1(\varepsilon,\phi) = 1-(0.0169-0.1900\ln(\varepsilon))\exp\left(-1.4892\varepsilon^{-0.4040}\phi\right)$
α_a	Diffuse irradiation on a gray surface with diffuse reflection	[27]	Same as above
α_a	Collimated irradiation with full-illumination ($\phi/2 \geq \gamma$) on a gray surface with diffuse reflection	[23]	$\alpha_a\left(\frac{\phi}{2} > \gamma\right) = 1-\Lambda_2(\alpha,\phi)\sum_{n=0}^{\infty}(1-\alpha)^{n+1}\left[1-\sin\left(\frac{\phi}{2}\right)\right]^n\sin\left(\frac{\phi}{2}\right)$ $\Lambda_2(\alpha,\phi) = 1-(0.0169-0.1900\ln(\alpha))\exp\left(-1.4415\alpha^{-0.4240}\phi\right)$
α_a	Collimated irradiation with partial-illumination ($\phi/2 < \gamma$) on a gray surface with diffuse reflection	[23]	$\alpha_a\left(\frac{\phi}{2} \leq \gamma\right) = 1-\Lambda_3(\alpha,\phi,\gamma)\left[(1-\alpha)F_{a-C}+\sum_{n=2}^{\infty}(1-\alpha)^n(1-F_{a-C})\sin\left(\frac{\phi}{2}\right)\left(1-\sin\left(\frac{\phi}{2}\right)\right)^{n-2}\right]$ $\Lambda_3(\alpha,\phi,\gamma) = D-E\exp(F\phi)$ $D = 0.0345\gamma^{-1.1447}\alpha^2-0.0414\gamma^{-0.8573}\alpha+1-1.7702\exp(-18.0990\gamma)$ $E = -3.2301\exp(-1.1420\gamma)\exp\left(-2.6635\gamma^{-0.0370}\alpha\right)$ $F = -2.2780\gamma^{-0.5690}\alpha^{\left(0.1330\gamma^2-0.2372\gamma-0.5434\right)}$

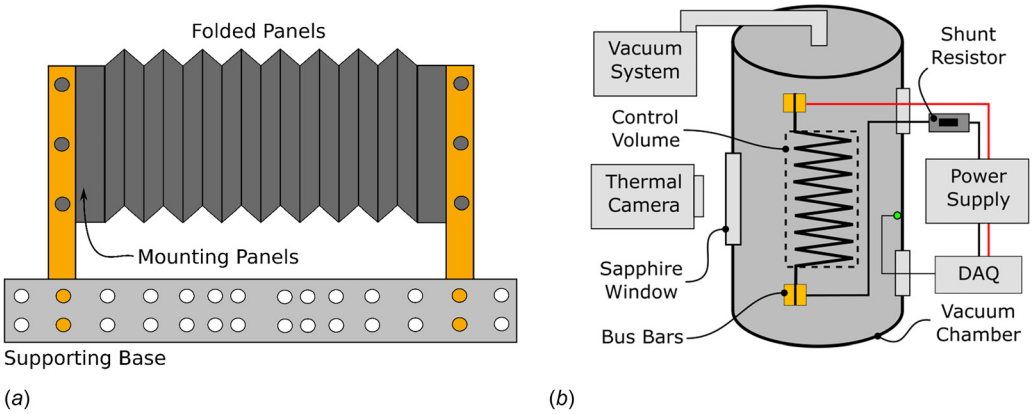

Fig. 2 (*a*) Schematic of folded stainless-steel samples with sixteen "folded panels" and two "mounting panels" constrained between two copper bus bars. Bus bars were positioned using a plastic supporting base with a hole pattern associated with desired angle positions and (*b*) schematic of the experimental setup in a vacuum. Steady-state temperatures were measured with an infrared camera through a sapphire window, while the voltage and current associated with Joule heating were measured to determine net radiative heat transfer after accounting for losses.

affect the geometry and positioning of the panels to achieve variable heat transfer control.

Experimental Methods

Experiments were performed to validate the models and assumptions utilized in the analytical predictions above. This experimentation was restricted to one of four possible irradiation/reflection modes, namely specular reflection with diffuse irradiation. Results from the experiment are compared to results from the analytical model to demonstrate the accuracy of the approach and models utilized.

Experimental Setup. An accordion tessellation was folded from a single piece of polished 18-8 stainless-steel shim stock (0.0254 mm thick) measuring 25.4 cm by 7.62 cm. The folded test piece had 16 panels (N_{panels}) with each panel measuring $W_P = 1.27$ cm in width and $L_P = 7.62$ cm in length, giving a length to width ratio of 6. Mounting panels (2.54 cm by 7.62 cm) remained unfolded on both ends with half of each mounting panel constrained between two vertical copper bus bars (Fig. 2(*a*)). The bus bars suspended the folded test piece vertically at one of the seven discrete fold angles ($\phi = \pi/9$, $\pi/6$, $\pi/4$, $\pi/3$, $\pi/2$, $11\pi/18$, π or 20 deg, 30 deg, 45 deg, 60 deg, 90 deg, 110 deg, 180 deg) using an electrically and thermally insulating base with preset holes. When the tessellation was positioned for testing, calipers were used to measure the opening distance of each individual V-groove at three different vertical points. These measurements were used to find the average V-groove angle ϕ and standard deviation.

The sample and fixture were placed at the center of a cylindrical vacuum chamber measuring 70 cm in diameter and 76.2 cm in length, as shown in Fig. 2(*b*). Wire leads were bolted to each copper bus bar and connected to a power supply through a vacuum feedthrough. A 7.5 cm diameter sapphire window on the vacuum chamber wall provided optical access to the chamber interior and a thermal camera (FLIR 6103, Wilsonville, OR) was used to measure the apparent temperature of the cavity openings. The vacuum chamber was pumped down to a pressure of 4×10^{-5} Torr which ensured that convective heat transfer losses were negligible [29]. Upon achieving the desired vacuum conditions, the power supply was activated and electrical current, measured via a shunt resistor of known resistance, was passed through the shim stock to heat the sample via Joule heating. A data acquisition system monitored the applied voltage across the full circuit throughout testing. The resulting Joule heating in the folded sample caused the temperature to increase above ambient conditions, eventually reaching steady-state, defined as a temperature change of less than 0.5 deg K over a 1 h period.

Apparent Temperature Measurement. Several parameters were required in order to determine the apparent temperature of the tessellation cavity openings (T_a) through infrared thermography, including the transmissivity of the sapphire viewing window, temperature of the surroundings, and apparent emissivity of the tessellation. A *T*-type thermocouple attached to the wall of the vacuum chamber with thermal epoxy (Duralco 132, Cotronics Corp., Brooklyn, NY) was used to record the temperature of the enclosure/surroundings. The spectral transmissivity of the sapphire window, available from the manufacturer (Lesker, part number: VPZL-450DUSW, Jefferson Hills, PA), was multiplied by the blackbody spectral irradiation $G\lambda_{,b}$ and integrated over 3–5 μm (wavelength range of the thermal camera) to find the band transmissivity of the sapphire window for irradiation from heated accordion samples (Eq. (5), assuming gray emission)

$$\tau_{3-5\,\mu\text{m}} = \frac{\int_{3\mu\text{m}}^{5\mu\text{m}} \tau_\lambda G_{\lambda,b} d\lambda}{\int_{3\mu\text{m}}^{5\mu\text{m}} G_{\lambda,b} d\lambda} \tag{5}$$

Using the spectral transmissivity from the manufacturer, the calculated band transmissivity (3–5 μm) of the window ranged from 0.81 to 0.85 for irradiation values based on source temperatures of 323 K and 423 K, respectively. A transmissivity of 0.83 was used for measurements as this corresponded to the average steady-state temperature of the sample for all tested conditions (~373 K). The impact of the transmissivity variation on the infrared measurement of the sample was accounted for by incorporating possible transmissivity variation with temperature into the infrared measurement uncertainty.

To verify the transmissivity value obtained using Eq. (5), a laboratory blackbody emitter (Landcal R1200P, Dronfield, UK) with an emissivity of 0.97 was placed directly behind the sapphire window, with the blackbody cavity opening oriented parallel to the sapphire window and heated to 573 K. The thermal camera was placed on the opposing side of the sapphire window and focused to the center of the blackbody cavity. The camera emissivity parameter was set to 0.97 and the external optics transmissivity setting in the camera software was varied until the temperature measurement of the camera was identical to the set temperature of the blackbody [30]. With the blackbody emitter set to 573 K, the external optics transmissivity setting in the camera software which

gave a measured temperature of 573 K with the thermal camera was also 0.85, equivalent to that obtained from Eq. (5).

To determine the apparent emissivity of the tessellation, the V-groove angle and the intrinsic absorptivity of the stainless-steel surface were used in the specularly reflecting, diffusely emitting V-groove apparent emissivity model [28] as reported in Table 1. The intrinsic, total hemispherical emissivity of the stainless-steel was measured three times with an SOC-100 emissometer and then averaged to give a value of 0.117. The obtained apparent emissivity value was used as the emissivity parameter in the thermal camera software, correcting the temperature of the cavity to account for the cavity effect.

Upon reaching steady-state conditions, temperature data were collected using the thermal camera across the vertical center of all 8 V-groove openings comprising the accordion fold. The temperature profile over all V-grooves was averaged to eliminate local irregularities (due to the specular nature of the surfaces), giving the average emitting temperature of the accordion tessellation for a given power input. Temperature profiles were collected at seven discrete total power levels (3.0, 3.5, 4.0, 4.5, 5.0, 5.5, and 6.0 W) for each angle mentioned previously.

The apparent emissivity model used in this study assumes isothermal panels comprising the cavity. Experimentally, the isothermal condition was not imposed exactly. However, the alternating nature of the accordion fold (i.e., the vertex of a V-groove on one side is the peak protrusion on the opposite side) likely results in a relatively uniform heat loss from any position on a panel, assuming a linear heat loss profile along the length of a panel [31]. This fact, combined with the use of a thermally conductive material, suggests that the panel surfaces are near isothermal when heated.

Experimental Losses. The results of the idealized analytical model (Eq. (4)) must account for experimental losses to enable a comparison between experimental and analytical results. To this end, an energy balance of the experimental setup, using the control volume indicated in Fig. 2(*b*), is defined in the first equality of Eq. (6). The net radiative heat transfer can be obtained with this energy balance by measuring the total power dissipation in the circuit (P_t) and quantifying the electrical power dissipated outside of the sample control volume (P_{loss}) as well as the heat transferred from the sample control volume by conduction into the copper bus bars (q_{loss}). Equation (6) is rearranged to give the cavity surface temperature as a function of circuit power, experimental loss, and cavity parameters as shown in Eq. (7)

$$\begin{aligned} q_{\text{rad}} &= P_t - P_{\text{loss}} - q_{\text{loss}} \\ &= (N_P - 1)\left[2W_P L_P \sin\left(\frac{\phi}{2}\right)\right]\varepsilon_a \sigma\left(T_a^4 - T_{\text{surr}}^4\right) \end{aligned} \tag{6}$$

$$T_a = \left\{\frac{P_t - P_{\text{loss}} - q_{\text{loss}}}{(N_P - 1)\left[2W_P L_P \sin\left(\frac{\phi}{2}\right)\right]\varepsilon_a \sigma} + T_{\text{surr}}^4\right\}^{\frac{1}{4}} \tag{7}$$

Electrical power losses outside of the sample control volume (P_{loss}) and nonradiative heat losses from the sample control volume (q_{loss}) must be calculated to obtain the apparent surface temperature using Eq. (7). Each of these losses was determined experimentally, as outlined below.

Power Losses. Electrical heating that occurs outside of the sample control volume must be quantified and subtracted from the total power dissipation to determine the electrical heating present in the stainless-steel sample. Power dissipation in the supporting circuitry is quantified with a sample heating efficiency (η), or the ratio of power dissipated within the control volume to the total power. In selecting a method to determine the heating efficiency, it was important to consider the resistive losses in the wires as well as the resistance losses in the electrical contacts including between the copper bus bars and the stainless-steel sample. To determine the power dissipation within the sample alone, an unfolded stainless-steel sample of length 30.5 cm was secured within the fixture with the power supply set to a voltage of 1 V. The resulting current (measured at the power supply) and total circuit resistance were recorded. The sample was then removed from the fixture and 2.5 cm of its length was cut from one end. The shortened sample was then secured again into the fixture, and the resulting current and resistance at 1 V were again recorded. This process was repeated until the total sample length between bus bars was reduced to approximately 1.5 cm. The total resistance of the circuit was then plotted as a function of sample length and a linear fit to this data ($R^2 = 0.994$) provided the relationship between total circuit resistance and sample length. The *y*-intercept of the linear fit gives the resistance of the circuit for a theoretical sample length of zero, or the resistance of the circuit outside of the control volume pictured in Fig. 2(*b*), including the contact resistance. The heating efficiency is defined as the ratio of power dissipated in the stainless-steel sample (P_s) divided by the total power dissipated in the full circuit (P_t), given by Eq. (8). Since the current is the same throughout the full circuit, the heating efficiency can be expressed as a ratio of resistances, as shown in Eq. (8), where R_s is the resistance of the stainless-steel sample and R_t is the resistance of the full circuit. For a sample length of 25 cm, used in all radiative experiments, the heating efficiency was found to be 61%. The heating efficiency multiplied by the total circuit power (P_t) gives the rate of heat generation within just the sample material, P_s

$$\eta = \frac{P_s}{P_t} = \frac{I^2 R_s}{I^2 R_t} = \frac{R_s}{R_t} \tag{8}$$

The heating efficiency (η) gives the ratio of power dissipated in the sample (including the mounting panels shown in Fig. 2(*a*)) as compared to the total circuit power. Since the mounting panels are not included in the control volume of Eq. (6) (as shown in Fig. 2(*b*)), the heat generated within the mounting panels must also be subtracted from the circuit power to give the heat generation within just the control volume. The sample length ratio (χ) is the ratio of sample volume that resides within the control volume (i.e., folded panels) to the total sample volume (i.e., folded and mounting panels). For a sample length of 25 cm, $\chi = 91\%$. The heat generated within just the sample control volume (or P_t–P_{loss}) may be determined by multiplying the heating efficiency (η) and sample length ratio (χ) by the total circuit power.

Thermal Losses. The thermal camera was used to quantify heat lost from the accordion sample by conduction through the mounting panels. The sample fold pattern and fixturing device were designed such that the sample contained a flat portion (1.25 cm in length) immediately adjacent to the copper bus bars on either side before the tessellation folds began (Fig. 2(*a*)). The flat mounting panels are exterior to the sample control volume for the analytical model (Fig. 2(*b*)). To find the conduction loss through these panels, the thermal camera recorded the temperature profile along a mounting panel at the control volume edge for use in Fourier's law. This conduction loss was then subtracted from the total heating power (Eq. (6)).

The power and heat loss terms just described are applied to Eq. (7), giving the final form for the prediction of the apparent surface temperature, Eq. (9). This predicted temperature was compared against the value obtained from the thermal camera. For this equation, k_{SS} is the thermal conductivity of 18-8 stainless-steel at 350 K (15 W m^{-1} K^{-1}) and A_{cond} is the heat conduction area of the sample (twice the cross-sectional area of the shim)

$$T_a = \left\{\frac{\eta\chi P_t - k_{SS} A_{\text{cond}} \frac{dT}{dx}}{\left[4W_P L_P \sin\left(\frac{\phi}{2}\right)\left(\frac{N_P}{2}\right)\right]\varepsilon_a \sigma} + T_{\text{surr}}^4\right\}^{\frac{1}{4}} \tag{9}$$

Table 3 Uncertainties of the measurements and parameters used in Eq. (9)

Parameter	Uncertainty (±)	Units	Source/notes
T_{surr}	1	K	Manufacturer provided, *T*-type thermocouple
W_P	1.3×10^{-5}	m	Caliper resolution uncertainty
L_P	1.0×10^{-3}	m	Ruler resolution uncertainty
k_{SS}	0.25	$Wm^{-1}K^{-1}$	Variance between 50 and 150 °C
P_t	7.5×10^{-3}	W	RMS propagation of voltage and current measurement uncertainties
ε	0.005	—	Standard deviation of three emissivity measurements
ε_a	0.01	—	RMS propagation of ϕ and ε uncertainty
dT/dx	55.67[a]	Km^{-1}	RMS propagation of camera temperature measurements and length measurement
η	3.80×10^{-7}	—	RMS propagation of line of best fit slope and intercept uncertainties
χ	0.015	—	RMS propagation of caliper measurement uncertainty
ϕ	0.055[a]	radians	Standard deviation of 24 angle measurements

[a]Uncertainties that vary with circuit power and cavity angle

Uncertainty

The Thermal Camera Uncertainty and Analytical Model Uncertainty sections outline the uncertainty estimations for the experimental temperature measurement made by the thermal camera and the analytical model (Eq. (9)).

Thermal Camera Uncertainty. The thermal camera uncertainty is a function of the uncertainties of the emissivity measurement, the transmissivity of the sapphire window, the temperature of the surroundings, and the inherent uncertainty within the camera. The total uncertainty of the camera measurements was calculated through a modification of the method of sequential perturbation, as follows [32]. A sample is heated in one of two extreme configurations: (1) an unfolded sample heated with the lowest tested power level (3 W) and (2) a folded sample positioned at the smallest fold angle (20 deg) heated at the largest power level (6 W). For both testing scenarios, each parameter (emissivity, transmissivity, and surrounding temperature) is adjusted individually in the camera software upward and then downward by the associated uncertainty of that parameter. The resulting change in the temperature readout is recorded, and the increase and decrease in temperature for a given parameter is averaged to find the camera temperature uncertainty for that parameter. For this work, the uncertainty of the surroundings is taken to be the uncertainty of a *T*-type thermocouple (±1 °C); emissivity uncertainty is taken to be the uncertainty of the intrinsic emissivity reflectometer measurement (±0.006); and the sapphire window uncertainty is equivalent to the difference between the highest and lowest transmissivity values calculated with Eq. (5) at the extreme sample temperatures encountered in the experiment (±2%). The inherent uncertainty of the camera was also accounted for, with manufacturer specifications indicating that the camera uncertainty is 2% of the temperature value. For these uncertainties, the greatest overall apparent temperature uncertainty is observed with the sample folded to π/9 (20 deg) and heated with the highest power level with a value of 3.25 °C. This uncertainty value is used as the uncertainty of the camera apparent temperature measurement for all power levels and cavity angles.

Analytical Model Uncertainty. The overall uncertainty of temperatures obtained using Eq. (9) is also calculated with the method of sequential perturbation. Essentially, each parameter is individually increased or decreased by its given uncertainty value to determine the sensitivity of the results of Eq. (9) with respect to each individual parameter. The root sum square of all sensitivity indices gives the total uncertainty of Eq. (9). The uncertainty of each parameter is listed in Table 3 along with the source from which this uncertainty is derived/obtained. Parameters not listed in Table 3 but present in Eq. (9) do not have an associated uncertainty.

Several of the parameters listed in Table 3, including P_t, dT/dx, η , ε_a, and χ, are calculated from combinations of more basic measurements. The uncertainties of these values are calculated with the root-mean-squared (RMS) methods, as designated in Table 3 [32]. Uncertainty values given in Table 3 marked with an asterisk vary with each power/angle combination, with the reported value being the maximum uncertainty.

Results

Net Radiative Heat Transfer. Results for the net radiative heat transfer from an accordion fold are normalized by the net radiative heat exchange at a cavity angle of π (flat condition), as given in Eq. (10), in order to allow for comparison across intrinsic emissivities

$$\Pi = \frac{q_{\text{rad},\phi}}{q_{\text{rad},\phi=180\,\text{deg}}} \tag{10}$$

Figures 3(*a*)–3(*c*) provide the normalized results of Eq. (4) evaluated for four different scenarios across the complete angle range: (1) diffuse reflector and diffuse irradiation, (2) specular reflector and diffuse irradiation, (3) diffuse reflector and collimated irradiation, and (4) specular reflector and collimated irradiation. For all results provided here, a collimated irradiation flux *G* of 1360 W/m^2 was used as an estimation of solar irradiation [33].

Figure 3(*a*) provides the normalized net radiative heat exchange as a function of ϕ for diffuse irradiation incident on a cavity with either diffuse or specular reflection for two different intrinsic emissivity values. To visualize the impact of the cavity effect, the net radiative heat transfer for a flat, black surface equivalent in size to $A_a(\phi)$ is provided. As the cavity angle decreases toward zero, the net radiative heat exchange for both specular and diffuse reflection decreases to zero. This indicates that the decrease in projected surface area always dominates relative to the increase in apparent radiative properties with decreasing cavity angle. For cases where the cavity effect is especially pronounced (i.e., highly reflective surfaces), the increase in apparent radiative properties and the decrease in surface area are nearly balanced, resulting in a relatively constant net radiative heat exchange for a large angle range. This behavior significantly concentrates the change in net radiative heat exchange to small cavity angles. As an example, a specularly reflecting tessellation with an intrinsic emissivity of 0.2 experiences a turn-down ratio (ratio of largest to smallest heat transfer) of 7.3 as the V-groove angle collapses from π/6 (30 deg) to π/60 (3 deg). For diffuse reflectors, the heat transfer reduction capability is diminished; a diffusely reflecting surface with an intrinsic emissivity of 0.2 has a turn-down ratio of 5.9 over the same cavity angle range. As the intrinsic emissivity of the surface increases toward black behavior, the net radiative heat transfer curve approaches that of the shrinking flat surface, decreasing the turn-down ratio potential for this angle range even further. For an intrinsic emissivity of 0.5, the tessellation is characterized by a turn-down ratio of 4.8 (specular) and 3.2 (diffuse) over the range of π/6 (30 deg) to π/60 (3 deg).

The normalized net radiative heat transfer for collimated irradiation and diffuse reflection is given in Fig. 3(*b*) for $\varepsilon = 0.2$ and

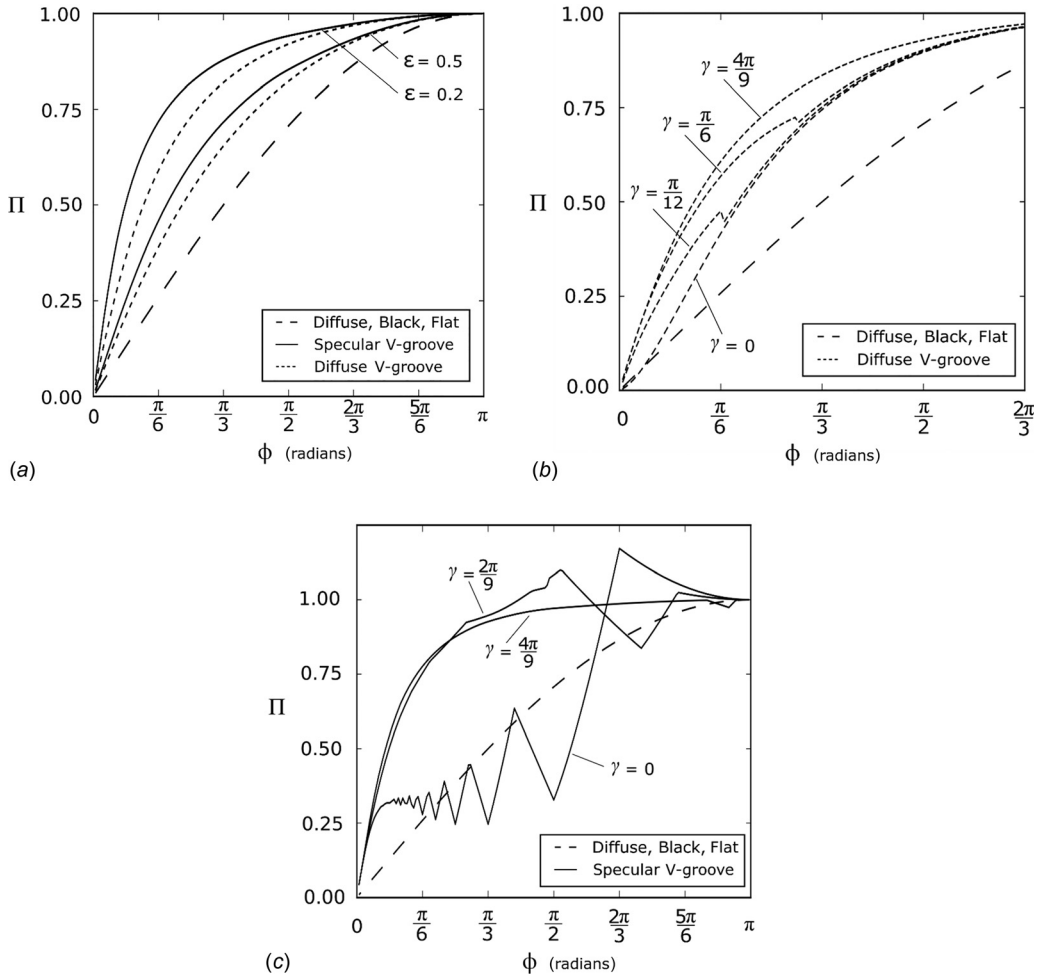

Fig. 3 (*a*) Normalized net radiative heat exchange Π as a function of ϕ for a diffusely irradiated accordion tessellation with specular or diffuse reflection for two different intrinsic emissivities. The "flat" case indicates a flat, black surface, equivalent in size to the apparent area at a given cavity angle, (*b*) normalized net radiative heat exchange Π as a function of ϕ for a diffusely reflecting accordion tessellation with collimated irradiation incident on the accordion tessellation at several angles γ, and (*c*) normalized net radiative heat exchange Π as a function of ϕ for a specularly reflecting accordion tessellation with collimated irradiation incident on the accordion tessellation at several angles γ.

four different collimation angles γ. The characteristic flat surface data are again plotted for comparison. When the cavity is fully illuminated ($\phi/2 \geq \gamma$), the normalized net radiative heat exchange for a given cavity angle is nearly equivalent across all possible collimation angles, giving behavior similar to the curve indicated by $\gamma = 0$ in Fig. 3(*b*). However, when the V-groove is partially illuminated ($\phi/2 < \gamma$), the normalized net radiative heat exchange increases above the fully illuminated case. This change in net radiative heat transfer behavior is caused by a rapid decrease in absorbing surface area with the onset of partial illumination, reducing the absorbing capability of the cavity. This effect delays the reduction in net radiative heat transfer as the cavity angle is collapsed, meaning that additional actuation is necessary to achieve the turn-down ratios experienced by the surfaces in Fig. 3(*a*). As the irradiation (G) increases, the possible turn down ratios likewise increase; the opposite behavior is observed as G is reduced. The normalized heat transfer may fall into negative values if the irradiation becomes sufficiently large ($G > 1800$), indicating that the net flow of energy is into the tessellation. Note that in Fig. 3(*b*), the horizontal axis is plotted over a reduced range ($\phi < 2\pi/3$) to magnify the behavior of the normalized net radiative heat transfer in the small angle range. The noncontinuous jump of Π observed when $\phi/2 = \gamma$ indicates discrepancies between the models for partial and full illumination at this transition (Table 2).

Results for the condition of collimated irradiation with specular reflection are depicted in Fig. 3(*c*) for a surface intrinsic emissivity of 0.2 evaluated at collimation angles of 0, $2\pi/9$ (40 deg), and $4\pi/9$ (80 deg). The combination of specular surfaces with collimated irradiation results in groups of parallel rays that follow similar reflection patterns [23]. Of the rays that are not absorbed by the cavity walls, a fraction (X' in Table 1) will experience n total reflections before exiting the cavity, while the remaining unabsorbed rays ($1 - X'$) will experience one less reflection ($n - 1$) before exiting the cavity [23]. The number of reflections n must be a whole number, and therefore, varies discretely as a function of V-groove angle. Likewise, the fraction X' is a function of n and also varies discretely as a function of V-groove angle. Further, X' cannot exceed unity as it is a fraction by definition. Therefore, X' must be rounded down whenever the computed value is greater than one, resulting in an additional source of noncontinuous behavior. When fully illuminated ($\phi/2 \geq \gamma$), the computed value of X' (via the equation given in Table 1) sometimes exceeds unity and the rounding operation, combined with the discrete nature of n, causes the net radiative heat transfer to vary in a noncontinuous fashion. This discontinuous behavior can appear dramatic (e.g., $\gamma = 0$), or exhibit smaller, "noisy" variations (e.g., $\gamma = 2\pi/9$ near $\phi = \pi/2$). When partially illuminated ($\phi/2 < \gamma$), the computed value of X' does not exceed unity, eliminating the noncontinuous

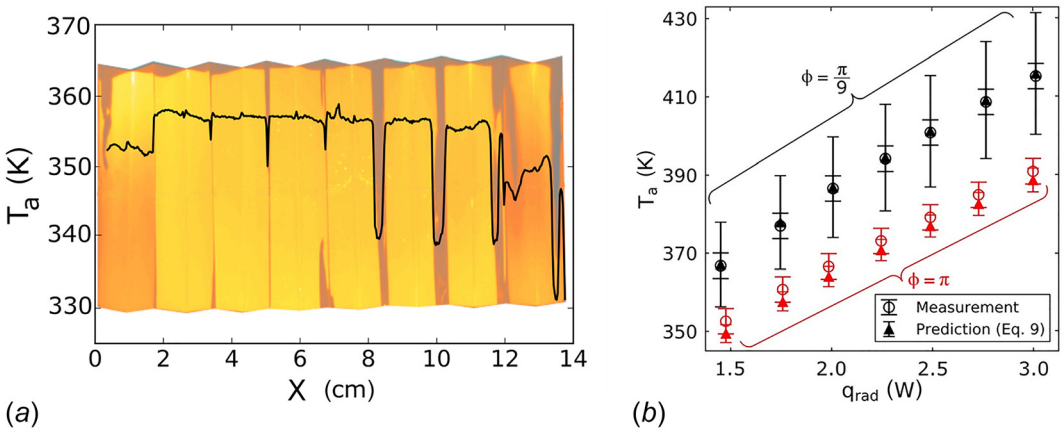

Fig. 4 (*a*) Temperature profile for a sample positioned at $\phi = \pi/2$ with a total heating power of 3 W. The thermal image from which this profile is derived is displayed behind the temperature profile, where the temperature profile was measured along a horizontal line across the vertical center of the tessellation and (*b*) comparison of experimental and analytical model temperature values. Experimental temperature measurements are derived from a thermal image of the heated surface (e.g., Fig. 4(*a*)). Predicted temperature values are determined with the analytical approach of Eq. (9). Data from two of the seven tested fold angles are provided with the uncertainties of each measurement.

influence of the rounding operation. For this case, the discrete variations in n and the resulting change in X' are coordinated such that the net radiative heat transfer varies in a continuous fashion, as shown by the $4\pi/9$ case in Fig. 3(*c*).

Unlike all other possible combinations of surface/irradiation conditions, specular reflection with collimated irradiation causes the net radiative heat transfer to drop below the characteristic flat case for small collimation angles. Further, specularly reflecting cavities with collimated irradiation experience drastic changes in net radiative heat transfer with respect to cavity angle, with larger variations occurring for small collimation angles and highly reflective surfaces. As an example, for irradiation normal to the surface ($\gamma = 0$) and an intrinsic surface emissivity of 0.2, the net radiative heat transfer experiences a turn-down ratio of 3.35 between the cavity angles of $2\pi/3$ (120 deg) and $\pi/2$ (90 deg). Although this turn-down ratio is small compared to the turn-down ratios seen in Fig. 3(*a*), this reduction in heat transfer occurs at much larger angles ($2\pi/3$ compared to $\pi/6$), resulting in a significant variation in heat transfer. Again, as the collimated irradiation flux (G) increases, the turn-down ratio likewise increases, and the normalized heat transfer may become negative in the small V-groove angle range. The presence of specular reflections also introduces normalized net radiative heat transfer values greater than unity in locations where the increase in apparent emissivity dominates the decrease in apparent surface area (e.g., $\phi > 2\pi/3$ and $\gamma = 0$).

Surface Temperature. For a thin, stainless-steel sample heated resistively in a vacuum environment, a typical infrared image and associated temperature profile is given in Fig. 4(*a*). Irregularities in temperature are observed near fold locations resulting in peaks or troughs in the temperature profile. These irregularities are due to warping and bending of the material near each bend and the specular behavior of the sample. Likewise, the average temperatures of individual cavities do not appear equivalent due to variation in cavity angles across the sample and discrepancies in cavity orientation with respect to the camera lens. Further, the V-groove cavities on the left-most or right-most edges show a smaller average temperature as compared to cavities in the middle region which is likely due to the presence of conductive heat losses. To mitigate these various effects, the temperature profile was averaged over all V-grooves comprising the accordion fold to obtain the steady-state apparent temperature measurement for a given cavity angle and circuit power.

The average steady-state temperature was measured with the thermal camera and calculated using Eq. (9) for seven different accordion fold angles at six power levels each. The results for both methods, with uncertainties, are given in Fig. 4(*b*) for the smallest and largest cavity angles ($\pi/9$ and π, respectively), where the x-axis of Fig. 4(*b*) is q_{rad} as calculated using Eq. (6). Table 4 gives the difference between the calculated apparent temperature using Eq. (9), the measured apparent temperature from the thermal camera (ΔT_a), and the percent difference between these two values, averaged across all tested total power levels for the seven cavity angles. The average uncertainties of the camera measurement and Eq. (9) are also provided in Table 4. The temperature results of both methods for all test cases fall within the bounds of uncertainty, as depicted in Fig. 4(*b*).

The uncertainty of the camera measurement is constant for all total power levels and cavity angles at a value of 3.25 °C. The

Table 4 Temperature error and uncertainties associated with each tested cavity angle averaged over all tested power levels. Average temperature difference (average ΔT_a) between the analytical model result (Eq. (9)) and the thermal camera temperature measurement and the associated average % Difference (relative to the camera measurement) are reported.

ϕ[a]	Average % difference	Average ΔT_a (deg K)	Average prediction uncertainty (deg K) (Eq. (9))	Average measurement uncertainty (deg K) (camera)
20 deg	0.4	0.46	13.44	3.25
30 deg	0.8	0.89	9.26	3.25
44 deg	3.3	3.76	4.96	3.25
56 deg	4.2	4.72	5.30	3.25
89 deg	1.2	1.23	4.00	3.25
109 deg	3.4	3.23	2.97	3.25
180 deg	2.7	0.03	2.70	3.25

[a]Angles provided in degrees for convenience; calculations should be performed in radians.

uncertainty of Eq. (9), however, varies with total circuit power and cavity angle (increasing uncertainty for larger power levels and for decreasing cavity angle). The largest uncertainty is ±15.2 deg K at a total power of 6 W and a cavity angle of $\pi/9$. The average prediction uncertainty across all cavity angles and power levels is ±6.1 deg K with a standard deviation of 3.74 deg K.

Discussion

As illustrated in Table 4 and Fig. 4(*b*), the net radiative heat transfer model developed in this work agrees with experimental results with a worst-case error of 4.2% averaged over all power levels. Likewise, Eq. (9) and thermal camera temperature measurements for all tested cavity angles and total powers agree within the uncertainties of both methods. This validates the results of the thermal model and suggests that the generic model is correct in predicting the net radiative heat exchange of an origami tessellation. This modeling approach may be used to predict the net radiative heat exchange of an isothermal, accordion tessellation when applied to a variety of thermal control scenarios and applications.

One purpose for this technology may be to provide variation in total net radiative heat transfer for thermal management. To this end, an efficient variable radiator should (1) provide a large change in net radiative heat transfer, (2) achieve this change in net radiative heat transfer over a small actuation range, and (3) minimize the material size and weight required to meet a given power requirement.

With regard to the first requirement, we see in Figs. 3(*a*)–3(*c*) that the net radiative heat exchange of an accordion tessellation may be varied from the full normalized value ($\Pi = 1$) to a value approaching zero, a significant variation in heat transfer, no matter how the material reflects or how the environment is heating the surface (diffuse or collimated irradiation). This versatile behavior is useful in applications where collimated and diffuse irradiation are both sometimes present, such as spacecraft thermal control.

Second, diffusely reflecting, high-emissivity ($\varepsilon > 0.5$) surfaces exposed to either diffuse or collimated irradiation exhibit a gradual change in net radiative heat transfer with changing cavity angle (Fig. 3(*a*)–3(*b*)). This slow change in heat transfer with position may not be ideal for applications that require rapid variation in heat transfer. However, the net radiative heat transfer of diffusely reflecting, low-emissivity ($\varepsilon < 0.2$) surfaces increases rapidly in the small angle ranges, achieving a turn-down ratio of 7.4 between the angles of $\phi \approx \pi/60$ to $\pi/6$. As such, reflecting surfaces may be more suited to applications requiring rapid variations in heat transfer. With regard to collimated irradiation and specular reflection (Fig. 3(*c*)), highly reflective surfaces ($\varepsilon < 0.2$) exposed to normal or near-normal collimated irradiation ($\gamma \approx 0$) show significant heat transfer variation, achieving a turn-down ratio of 3.35 ($\varepsilon = 0.2$) for a range of relatively large V-groove angles $2\pi/3 - \pi/2$ (120 deg – 90 deg). As the collimation angle increases, this same turn-down capability is possible but for a range of angles much closer to a fully collapsed condition ($\pi/6 - \pi/60$).

Finally, an efficient variable radiator should require minimal volume and mass to emit a given heat load. As an example, diffusely reflecting, highly reflective surfaces ($\varepsilon < 0.2$) show significant variation in heat transfer for very small cavity angles ($\phi < \pi/6$, Fig. 3(*a*)). However, the emissivity of these surfaces is quite low and the apparent area is very small compared to the total area, indicating that significantly large radiators would be required to reject a given heat load. The low emissivity values found in most of the highly variable surfaces and the existence of rapid heat transfer decrease in very small cavity angles is an impediment to utilizing these devices in an application such as aerospace where weight must be minimized. However, a specular surface exposed to normal collimated irradiation exhibits significant variation for large cavity angles ($\phi > \pi/2$) even as the emissivity is increased to larger values (e.g., $\varepsilon > 0.5$). As such, specular surfaces utilized in the presence of collimated irradiation show significant abilities to vary net radiative heat transfer while minimizing the weight necessary to reject a given heat load. Finally, a perfectly black surface shows significant variation in net radiative heat transfer while minimizing the amount of area required to emit a given heat load although the surface must be actuated over the full range of cavity angles to achieve this variation.

These results also indicate the utility of an actively controlled origami surface in maintaining or controlling the apparent emitting temperature of a surface. As shown in Fig. 4(*b*) and the net radiative heat transfer curves in Figs. 3(*a*)–3(*c*), the emission from an adapting surface may be tailored such that the infrared signature of the surface and the apparent temperature of the surface may be controlled to a desired value. This includes maintaining a surface at a constant apparent temperature or varying the apparent temperature so as to hide the true emitting temperature of the surface.

The accordion tessellation may also be utilized in a constant-area scenario. In this case, only a portion of the fold is exposed to the surroundings, while the remainder may be shielded. As the fold collapses or expands, the viewing window between the tessellation and the surroundings remains the same. This behavior causes the area terms of Eq. (1) to remain constant, removing the effect of the collapsing area from the net radiative heat transfer. This scenario would cause the net radiative heat transfer to *increase* as the cavity angle is decreased. A disadvantage with this application is the requirement to store tessellation material without exposing it to the surroundings, potentially increasing the weight of the device substantially.

Several other origami tessellations are of possible interest as variable radiators [18]. One such tessellation is Barretto's mars, a fold which collapses to one side, resulting in directional behavior that is concentrated to non-normal angles. This tessellation collapses to a finite area, eliminating the decrease of net radiative heat transfer to zero. Another possible tessellation is a modified, constant-projected-area accordion tessellation. This tessellation maintains a given projected area throughout its actuation but can only collapse to a finite cavity angle, limiting its increase in net radiative heat transfer.

Conclusions

An expression to predict the net radiative heat transfer of an isothermal accordion origami tessellation (Eq. (4)), after accounting for experimental losses and averaging over all tested power levels (Eq. (7)), exhibits a 4.2% relative error or less when compared with experimental results. This equation may be used for all possible cavity angles, collimation angles, and intrinsic radiative surface properties as well as for diffuse or specular reflection and collimated and/or diffuse irradiation. A survey of the analytical results indicates that a specularly reflecting tessellation exposed to diffuse irradiation experiences large reductions in net radiative heat transfer for small cavity angle variations, achieving turn-down ratios greater than seven over a cavity angle range of $\pi/6$ for highly reflective surfaces. Diffuse reflectors with low intrinsic emissivities behave in a similar fashion but exhibit smaller turn-down ratios over a similar cavity angle range. When exposed to collimated irradiation, the turn-down ratio of diffuse reflectors is further reduced over the same cavity angle range. However, when exposed to collimated irradiation, specular surfaces experience erratic behavior, with widely varying net radiative heat transfer over relatively small changes in cavity angle for surfaces with low to moderately high emissivity. For this scenario, turn-down ratios of 3.35 and greater are possible for large cavity angles ($\phi > \pi/2$). When actuated dynamically, an accordion tessellation would provide active control of radiative heat losses, allowing for real-time thermal control in scenarios where radiative heat transfer is dominant.

Acknowledgment

The authors would like to acknowledge the assistance of Mitch Blanc and Nathan Collins for their assistance in the experimental methods used in this work.

Funding Data

- NASA Space Technology Research Fellowship, National Aeronautics and Space Administration (NNX15AP49H, Funder ID. 10.13039/100000104).
- National Science Foundation (1749395, Funder ID. 10.13039/100000001).

Nomenclature

A_a = apparent area of the accordion tessellation (m^2)
$A_{a,\text{proj}}$ = apparent projected area normal to collimated irradiation (m^2)
A_{cond} = 2× sample cross-sectional area (m^2)
dT/dx = conductive loss temperature gradient (K m^{-1})
G = collimated irradiation heat flux (W m^{-2})
$G_{\lambda,b}$ = spectral irradiation from a black surface (W m^{-2})
I = current (A)
k_{ss} = thermal conductivity of stainless-steel (W m^{-1} K^{-1})
L_P = length of a panel (m)
n = largest number of reflections experienced by collimated rays in a specular cavity
N_P = number of panels
P_{loss} = power dissipated in the circuit outside of the control volume (W)
P_s = power dissipated in the stainless-steel sample (W)
P_t = total power dissipated in the circuit (W)
q_{abs} = irradiation absorbed by the tessellated surface (W)
q_e = heat emitted by tessellated surface (W)
q_{loss} = heat loss via conduction (W)
q_{rad} = net radiative heat loss from the tessellated surface (W/m)
R_s = resistance of the stainless-steel surface (Ω)
R_t = resistance of the total circuit including the stainless-steel surface (Ω)
T_a = apparent temperature of the tessellation opening (K)
T_{surr} = temperature of the surroundings (K)
x = horizontal location on tessellation (cm)
W_P = width of a tessellation panel (m)
X' = fraction of unabsorbed, collimated rays that reflect n times in a specular cavity
α_a = apparent absorptivity
γ = collimated irradiation angle (radians)
ε = intrinsic emissivity of the sample material
ε_a = apparent emissivity
η = sample heating efficiency
τ_λ = spectral, hemispherical transmissivity of the sapphire window
$\tau_{3\text{-}5\ \mu\text{m}}$ = transmissivity of the sapphire window over 3–5 μm band
ϕ = cavity angle (radians)
χ = sample length ratio
ΔT_a = temperature difference between analytical and experimental results (deg K)
Π = normalized net radiative heat transfer

References

[1] Gilmore, D. G., 2002, *Spacecraft Thermal Control Handbook*, The Aerospace Corporation, El Segundo, CA.
[2] Karam, R. D., 1998, *Satellite Thermal Control for System's Engineers*, American Institute of Aeronautics and Astronautics, Cambridge, UK.
[3] Grob, L. M., and Swanson, T. D., 2000, "Parametric Study of Variable Emissivity Radiator Surfaces," *Space Technology and Applications International Forum*, M. S. El-Genck, ed., American Institute of Physics, Albuquerque, NM.
[4] Hengeveld, D. W., Mathison, M. M., Braun, J. E., Groll, E. A., and Williams, A. D., 2010, "Review of Modern Spacecraft Thermal Control Technologies," HVACR Res., **16**(2), pp. 189–220.
[5] Hale, J. S., DeVries, M., Dworak, B., and Woollam, J. A., 1998, "Visible and Infrared Optical Constants of Electrochromic Materials for Emissivity Modulation Applications," Thin Solid Films, **313–314**, pp. 205–209.
[6] Franke, E. B., Trimble, C. L., Hale, J. S., Schubert, M., and Woollam, J. A., 2000, "Infrared Switching Electrochromic Devices Based on Tungsten Oxide," J. Appl. Phys., **88**(10), p. 5777.
[7] Kislov, N., 2003, "All-Solid-State Electrochromic Variable Emittance Coatings Thermal Management Space," AIP Conf. Proc., **654**, pp. 172–179.
[8] Larsson, A.-L., and Niklasson, G. A., 2004, "Infrared Emittance Modulation of All-Thin-Film Electrochromic Devices," Mater. Lett., **58**(20), pp. 2517–2520.
[9] Biter, W., Hess, S., Oh, S., Douglas, D., and Swanson, T., 2005, "Electrostatic Radiator for Satellite Thermal Control," Aerospace Conference, Big Sky, MT, Mar. 5–12, pp. 781–790.
[10] Demiryont, H., Shannon, K. I., and Ponnappan, R., 2006, "Electrochromic Devices for Satellite Thermal Control," *Space Technology and Applications International Forum*, American Institute of Physics, Albuquerque, NM, Feb. 12–16, pp. 64–73.
[11] Demiryont, H., and Moorehead, D., 2009, "Electrochromic Emissivity Modulator for Spacecraft Thermal Management," Sol. Energy Mater. Sol. Cells, **93**(12), pp. 2075–2078.
[12] Benkahoul, M., Chaker, M., Margot, J., Haddad, E., Kruzelecky, R., Wong, B., Jamroz, W., and Poinas, P., 2011, "Thermochromic VO_2 Film Deposited on Al With Tunable Thermal Emissivity for Space Applications," Sol. Energy Mater. Sol. Cells, **95**(12), pp. 3504–3508.
[13] Voti, R. L., Larciprete, M. C., Leahu, G., Sibilia, C., and Bertolotti, M., 2012, "Optimization of Thermochromic VO_2 Based Structures With Tunable Thermal Emissivity," J. Appl. Phys., **112**(3), p. 034305.
[14] Voti, R. L., Leahu, G. L., Larciprete, M. C., Sibilia, C., and Bertolotti, M., 2014, "Photothermal Characterization of Thermochromic Materials for Tunable Thermal Devices," Int. J. Thermophys., **36**(5–6), pp. 1004–1015.
[15] Hill, S. A., Kostyk, C., Moril, B., Notardonato, W., Rickman, S., and Swanson, T., 2012, "NASA Technology Roadmaps, TA 14: Thermal Management Systems," National Aeronautics and Space Administration, Washington, DC, accessed Jan. 17, 2019, https://www.nasa.gov/sites/default/files/atoms/files/2015_nasa_technology_roadmaps_ta_14_thermal_management_final.pdf
[16] Blanc, M. J., Mulford, R. B., Jones, M. R., and Iverson, B. D., 2016, "Infrared Visualization of the Cavity Effect Using Origami-Inspired Surfaces," ASME J. Heat Transfer, **138**(2), p. 020901.
[17] Mulford, R. B., Jones, M. R., and Iverson, B. D., 2016, "Dynamic Control of Radiative Surface Properties With Origami-Inspired Design," ASME J. Heat Transfer, **138**(3), p. 032701.
[18] Iverson, B. D., Mulford, R. B., Lee, E. T., and Jones, M. R., 2018, "Adaptive Net Radiative Heat Transfer and Thermal Management With Origami-Structured Surfaces," 16th International Heat Transfer Conference, Heat and Mass Transfer Society of China, Beijing, China, Aug. 10–15, Paper No. IHTC16-23600.
[19] Sparrow, E. M., and Albers, L. U., 1960, "Apparent Emissivity and Heat Transfer in a Long Cylindrical Hole," ASME J. Heat Transfer, **82**(3), pp. 253–255.
[20] Sparrow, E. M., and Lin, S. H., 1962, "Absorption of Thermal Radiation in a V-Groove Cavity," Int. J. Heat Mass Transfer, **5**(11), pp. 1111–1115.
[21] Sparrow, E. M., 1965, "Radiant Emission, Absorption, and Transmission Characteristics of Cavities and Passages," National Aeronautics and Space Administration, Washington, DC, Report No. 55.
[22] Prokhorov, A. V., Hanssen, L. M., and Mekhontsev, S. N., 2009, "Calculation of the Radiation Characteristics of Blackbody Radiation Sources," Exp. Methods Phys. Sci., **42**, pp. 181–240.
[23] Mulford, R. B., Collins, N. S., Farnsworth, M. S., Jones, M. R., and Iverson, B. D., 2018, "Total Hemispherical Apparent Radiative Properties of the Infinite V-Groove With Specular Reflection," Int. J. Heat Mass Transfer, **124**, pp. 168–176.
[24] Mulford, R. B., Collins, N. S., Farnsworth, M. S., Jones, M. R., and Iverson, B. D., 2018, "Total Hemispherical Apparent Radiative Properties of the Infinite V-Groove With Diffuse Reflection," J. Thermophys. Heat Transfer, **32**(4), pp. 1108–1112.
[25] Evans, T. A., Lang, R. J., Magleby, S. P., and Howell, L. L., 2015, "Rigidly Foldable Origami Gadgets and Tessellations," R. Soc. Open Sci., **2**(9), p. 150067.
[26] Daws, L. F., 1954, "The Emissivity of a Groove," Br. J. Appl. Phys., **5**(5), pp. 182–187.
[27] Ohwada, Y., 1988, "Mathematical Proof of an Extended Kirchhoff Law for a Cavity Having Direction-Dependent Characteristics," J. Opt. Soc. Am., **5**(1), pp. 141–145.
[28] Modest, M. F., 2013, "Enclosures With Partially-Specular Surfaces," *Radiative Heat Transfer*, Academic Press, London, pp. 202–213.
[29] Guy, W. W., and Ellis, W. E., 1963, "Vacuum Chamber Heat Transmission Analysis," National Aeronautics and Space Administration, Houston, TX, Report No. NASA-TM-X-65036.
[30] ASTM, 2014, "Measuring and Compensating for Transmittance of an Attenuating Medium Using Infrared Imaging Radiometers," ASTM, West Conshohocken, PA, Standard No. E1897-14.
[31] Sparrow, E. M., Gregg, J. L., Svel, J. V., and Manos, P., 1961, "Analysis, Results and Interpretation for Radiation Between Some Simply-Arranged Gray Surfaces," ASME J. Heat Transfer, **83**(2), pp. 207–214.
[32] Figliola, R. S., and Beasley, D. E., 2006, *Theory and Design for Mechanical Measurements*, Wiley, Hoboken, NJ.
[33] Kopp, G., and Lean, J. L., 2011, "A New, Lower Value of Total Solar Irradiance: Evidence and Climate Significance," Geophys. Res. Lett., **38**(1), p. L01706.